In-situ Nanostructuring and Stabilization of Polycrystalline Copper by an Organic Salt Additive Promotes Electrocatalytic CO_2 Reduction to Ethylene

Arnaud Thevenon, Alonso Rosas-Hernández, Jonas C. Peters*, Theodor Agapie*

Division of Chemistry and Chemical Engineering and Joint Center for Artificial Photosynthesis, California Institute of Technology, Pasadena, California 91125, United States

Table of Contents

Materials. **4**

Synthetic Procedures **4**

Electrochemical Measurements. **5**

X-ray photoelectron spectroscopy (XPS) **6**

Atomic Force Microscopy (AFM) **6**

Scanning Electron Microscopy (SEM) and Energy Dispersive X-ray (EDX) **7**

X-ray Diffraction (XRD) **7**

Supporting Figures and Tables **7**

Table S1. Faradaic efficiency (%) for CO_2RR products without and with 10 mM **1-Br$_2$**. **8**

Figure S1. ^{1}H NMR spectrum of **1-Br$_2$**. **8**

Figure S2. GC-MS analyses and ^{1}H NMR spectra products collected during CO_2RR with natural abundance and ^{13}C-enriched CO_2-saturated $KHCO_3$. **9**

Figure S3. Chronoamperograms of electrolysis with **1-Br$_2$** at different potentials. **10**

Table S2. Faradaic efficiency (%) for CO_2RR products with **1-Br$_2$** at different potentials. **10**

Table S3. Faradaic efficiency (%) for CO_2RR products with **1-Br$_2$** at different concentration **11**

Figure S4. Chronoamperograms of electrolysis with **1-Br$_2$** at different concentration. **11**

Figure S5. Plot of the Faradaic efficiencies for gaseous products over 10 h. **12**

Figure S6. Chronoamperograms for 10 h of electrolysis. **12**

Figure S7. Plot of the Faradaic efficiencies for gaseous products over 43 h. **13**

Figure S8. Chronoamperograms for 43 h of electrolysis. **13**

Figure S9. Normalized X-ray photoelectron spectra of Cu after electrolysis. **14**

Figure S10. Proposed structures and ^{1}H NMR spectrum of the dimers. **15**

Figure S11. ^{1}H-^{1}H COSY spectrum of the dimers. **16**

Table S4. Faradaic efficiency (%) towards different products under different conditions. **17**

Figure S12. Rotating disk electrode results under N_2 ..... **18**

Figure S13. Rotating disk electrode results under CO_2 ..... **18**

Figure S14. Ex-situ AFM images before and after catalysis with and without **1-Br$_2$** **18**

Figure S15. Typical normalized XRD pattern of (a) an electropolished Cu electrode; post catalysis Cu electrodes (b) without additive; (c) with **1-Br$_2$** **19**

Figure S16. Ex-situ AFM images of the same post catalysis Cu electrode after 43 h of electroreduction at -1.07 V (a) before and (b) after the extraction of the organic film. **19**

Figure S17. Ex-situ AFM images of copper electrode in presence of KBr. **20**

Table S5. Faradaic efficiency (%) for CO_2RR products and hydrogen with KBr. **20**

Table S6. Faradaic efficiency (%) for CO_2RR products and hydrogen with 1-X_2. ..... **21**

Figure S18. *Ex-situ* AFM images of Cu electrodes with (a) **1-Cl$_2$**; (b) **1-(OTf)$_2$**; (c) **1-I$_2$**; (d) **1-I$_2$** after extracting the organic film. **22**

Table S7 Faradaic efficiency (%) for CO_2RR products after extracting the film and submitting the same electrode with no **1-Br$_2$** in the electrolyte. **22**

Table S8. Faradaic efficiency (%) for CO_2RR products with **1-Br$_2$** and submitting the same electrode with no **1-Br$_2$** in the electrolyte. **23**

Dimerization Mechanism **24**

Figure S19. Cyclic voltammogramms of **1-Br$_2$** under CO_2. ..... **25**

Figure S20. ^{1}H NMR spectra of the extracted films obtained after CV experiments. **26**

Figure S21. Pictures of the electrolyte containing **1-Br$_2$** before and after catalysis. **26**

Figure S22. Stack of ^{1}H NMR spectra of electrolyte after catalysis, the organic precipitate extracted from the counter electrode, and the organic film extracted from the Cu electrode. **27**

Figure S23. Cyclic voltammograms on a glassy carbon electrode of **1-Br$_2$**..... **27**

Reactivity studies of 1˙-Br with CO_2.....**28**

Figure S24. Visible spectra of **1-Br$_2$** and **1˙-Br** in water..... **28**

Figure S25. Visible spectra of **1˙-Br** under N_2 and under CO_2 in 0.1 M $KHCO_3$. **28**

Figure S26. EPR spectra of **1˙-Br** under CO_2 and N_2..... **29**

References.....**30**

Materials

All solvents and reagents were obtained from commercial sources (Aldrich and Merck) and used as received, unless stated otherwise. Phenanthrolinium additives were synthesized according to previous literature procedures,[1–5] and recrystallized from MeOH/Ether (1:5) prior to use.

Copper foil (product number 266744, 99.999% Cu, 25 mm × 50 mm × 1 mm), phosphoric acid (85%, TraceSelect), potassium carbonate (99.995%), potassium hydroxide (semiconductor grade, 99.99% trace metals basis) and $^{13}CO_2$ (99 atom % ^{13}C, <3 atom % ^{18}O) were purchased from Sigma-Aldrich. Carbon rods (99.999% C) were purchased from Strem Chemicals. Natural abundance CO_2 (Research grade) was purchased from Airgas. Deuterium dioxide (D 99.96%), d-chloroform (D 99.8%) and d-dimethylsulfoxide (D 99.8%) were purchased from Cambridge Isotope Laboratories.

Water was purified by a Nanopure Analytical Ultrapure Water System (Thermo Scientific) or a Milli-Q Advantage A10 Water Purification System (Millipore) with specific resistance of 18.2 MΩ·cm at 25 °C.

^1H and ^{13}C NMR spectra were recorded on a Bruker 400 MHz instrument with a prodigy broadband cryoprobe. Shifts were reported relative to the residual solvent peak.

Upon receiving, copper foil was polished to a mirror-like finish using alumina paste (0.05 μm, Buehler) followed by rinsing and sonicating in water to remove residual alumina. Before each experiment, the copper foil was electropolished using a method similar to the one employed by Kuhl et al.[6] In an 85% phosphoric acid bath, +2.1 V versus a carbon rod counter electrode was applied to the Cu foil for 5 minutes and the foil was subsequently washed with ultra-pure water and dried under a stream of nitrogen gas.

Potassium bicarbonate electrolyte ($KHCO_3$(aq), 0.1 M) was prepared by sparging an aqueous solution of potassium carbonate (K_2CO_3(aq), 0.05 M) with CO_2 for at least 1 hour prior to electrolysis. This process converts K_2CO_3 into $KHCO_3$ and saturates the electrolyte solution with CO_2. The proper organic salt additive was added to the 0.1 M $KHCO_3$(aq) catholyte (unless otherwise stated [additive] = 10 mM) whereas 0.1 M $KHCO_3$(aq) without any additives was used as the anolyte.

Synthetic Procedures

Synthesis of N,N'-ethylene-phenanthrolinium dibromide (1-Br_2)

In a round bottom flask charged with a magnetic stir bar, phenanthroline (500 mg, 2.8 mmol, 1 equiv.) was dissolved in dibromoethane (5 mL, 67.4 mmol, > 24 equiv.) and the final mixture was heated to 110 °C for 18 h. The precipitate formed was collected by filtration and washed with hexane (3 x 10 mL) and acetone (3 x 10 mL) to afford the final product. Yield: 970 mg (94 %, 2.6 mmol). ^1H and ^{13}C NMR spectra were in accordance with reported values.[1–3]

Synthesis of N,N'-ethylene-phenanthrolinium ditriflate [1-$(OTf)_2$]

In a flame dried Schlenk flask charged with a magnetic stir bar, under N_2 and in absence of light, phenanthrolinium dibromide (200 mg, 0.5 mmol, 1 equiv.) was dissolved in dry acetonitrile (10 mL). Silver triflate (280 mg, 1.0 mmol, 2 equiv.) was added and the final

mixture was stirred for 18 h, at 25 °C. The AgBr precipitate was discarded by filtration. The solvent was evaporated yielding a brown powder. Yield: 212 mg (84 %, 0.4 mmol). ^{1}H and ^{13}C NMR spectra were in accordance with reported values.[4]

Synthesis of N,N'-ethylene-phenanthrolinium dichloride
Phenanthrolinium dibromide (100 mg, 0.25 mmol, 1 equiv.) was dissolved in 1.0 mL of water and eluted several times through an ion exchange resin (Amberlite IRA-400 chloride form). Yield: 70 mg (100 %, 0.25 mmol). ^{1}H and ^{13}C NMR spectra were in accordance with reported literatures.[5]

Synthesis of N,N'-ethylene-phenanthrolinium diiodide
Phenanthrolinium dibromide (100 mg, 0.27 mmol) was dissolved in 10 mL of water and eluted several times through a pre-washed ion exchange resin (Amberlite IRA-400 chloride form) with HI. After removal of the water under vacuum, 112 mg of a red solid were obtained (91% yield). ^{1}H NMR (400 MHz, D_2O) δ (ppm): 8.78 (dd, $^{2}J_{H-H}$ = 4.5 Hz, $^{3}J_{H-H}$ = 1.7 Hz, 2H), 8.10 (dd, $^{2}J_{H-H}$ = 8.31 Hz, $^{3}J_{H-H}$ = 1.7 Hz, 2H), 7.53 (m, 2H), 7.45 (s, 2H), 4.42 (m, 1H), 3.88 (m, 1H), 3.68 (m, 2H), 3.29 (m, 2H). ^{13}C NMR (101 MHz, D_2O) δ (ppm): 148.2 (s), 141.1 (s), 137.7 (s), 127.9 (s), 125.9 (s), 123.6 (s), 46.3 (s), 44.1 (s), 32.9 (s).

Electrochemical Measurements

Chronoamperometry measurements were carried out in a custom-made PEEK flow cell setup similar to the one reported by Ager et al.[7] using a copper foil as the working electrode and a platinum foil as the counter electrode. The cathode compartment was separated from the anode compartment by a Selemion AMV anion-exchange membrane (AGC Engineering Co.). All potentials were measured versus a leakless Ag/AgCl reference electrode (Innovative Instruments) with an outer diameter of 5 mm that was inserted into the cathode compartment. The reference electrode was calibrated against ferrocenecarboxylicacid in a 0.2 M phosphate buffer solution at pH 7.0 (+0.239 V vs. Ag/AgCl). All electrochemical measurements were carried out using a Biologic VMP3 multichannel potentiostat.

Potentiostatic electrochemical impedance spectroscopy (PEIS) measurements were carried out prior to each electrolysis experiment to determine the Ohmic resistance of the flow cell. The impedance measurements were carried out at frequencies ranging from 200 kHz to 100 MHz to measure the solution resistance. A Nyquist plot was plotted and in the high-frequency part a linear fit was performed and the axis intersection was calculated. The value of this intersection represents the Ohmic resistance of the cell. An average of 3 measurements was taken to calculate the value of R. Typically, small resistances were measured, ranging from 40 to 60 Ω.

All chronoamperometric experiments were performed for 65 min at 25 °C using CO_2-saturated 0.1 M $KHCO_3$ as electrolyte. The potentiostat was set to compensate for 85 % of the Ohmic drop, with the remaining 15 % being compensated for after the measurements. The effluent gas stream coming from the flow cell (5 mL/min) was flowed into the sample loops of a gas chromatograph (GC-FID/TCD, SRI 8610C, in Multi Gas 5 configuration) equipped with HayeSep D and Molsieve 5A columns. Methane, ethylene, ethane and carbon monoxide were detected by a methanizer-flame ionization detector (FID) and the hydrogen was detected by a thermal conductivity detector (TCD). Every 15 minutes, 2 mL of gas was sampled to determine the concentration of gaseous products. After electrolysis, the liquid products in both catholytes and anolytes were quantified by both HPLC (Thermo Scientific Ultimate 3000) and ^{1}H NMR.

For ^{1}H NMR, solutions containing 90% electrolyte and 10% D_2O (v/v) with internal standard (N,N-dimethylformamide or dimethylsulfoxide) were prepared and measured using a water suppression technique on a Bruker 400 MHz NMR spectrometer.

All potentials were converted from the Ag/AgCl scale to the reversible hydrogen electrode (RHE) scale by using $V_{RHE} = V_{(Ag/AgCl)measured} - 0.197 - 0.059 \times pH$, where V_{RHE}, $V_{(Ag/AgCl)measured}$ and pH are potential vs RHE, measured potential vs Ag/AgCl reference electrode and pH of the electrolyte (6.8).

Cyclic voltammetry (CV) measurements were recorded at 25 °C using a one-compartment cell with a Cu or a glassy carbon disk working electrodes (diameter 3 mm), Pt counter electrode, and a Ag/AgCl reference electrode. The electrolyte solutions were either CO_2 or N_2 saturated 0.1 M $KHCO_3$ in H_2O and were stirred during all measurements.

For isotopic labeling experiments the same experimental configurations as described above were employed except $KH^{13}CO_3(aq)$ solution and $^{13}CO_2$ were used as the electrolyte and CO_2 source, respectively. To prepare the 0.1 M $KH^{13}CO_3(aq)$ solution, 50 mL of nanopure water was sparged with nitrogen for 1 h and was added to potassium hydroxide (0.32 g containing 12.6% water) in a Schlenk flask under nitrogen atmosphere. The headspace was evacuated for a few seconds, and $^{13}CO_2$ was introduced. The solution was stirred vigorously for 5 h and an aliquot was extracted to make sure the pH was ~7. The solution was then added to a pre-evacuated 4 mL vial containing **1-Br₂** to yield the final electrolyte solution of 0.1 M $KH^{13}CO_3(aq)$ and 10 mM **1-Br₂**. During the electrolysis, $^{13}CO_2$ was introduced from the bottom of the flow cell at 5 ml/min. The outlet was connected to the inlet of the sample loop of the GC-FID/TCD for quantitative analyses every 15 min. To collect the gaseous products for GC-MS and NMR analyses, the outlet of the GC sample loops was connected to a syringe with rubber plunger pulled by a syringe pump set to the same rate as the gas flow. GC-MS analyses was performed using an Agilent 7820A GC coupled with a 5977E MS with a heated cold quadrupole detector and a capillary CarbonPLOT column for identification of the mass fragmentation of ethylene. The background signal was subtracted.

X-ray photoelectron spectroscopy (XPS)

X-ray photoelectron spectroscopy (XPS) data were collected using a Surface Science Instruments M-Probe ESCA controlled by Hawk Data Collection software (Service Physics, Bend OR; V7.04.04). The monochromatic X-ray source was the Al Kα line at 1486.6 eV, directed at 35° to the sample surface (55° off normal). Emitted photoelectrons were collected at an angle of 35° with respect to the sample surface (55° off normal) by a hemispherical analyzer. The angle between the electron collection lens and X-ray source is 71°. Low-resolution survey spectra were acquired between binding energies of 1-1000 eV. Higher-resolution detailed scans, with a resolution of ~0.8 eV, were collected on individual XPS lines of interest. The sample chamber was maintained at $< 2 \times 10^{-9}$ Torr. The XPS data were analyzed using the CasaXPS software. Copper foils after electropolishing or electrolysis were rinsed with copious amount of water, dried under a stream of nitrogen and immediately transferred to a nitrogen glove box before XPS measurements.

Atomic Force Microscopy (AFM)

All AFM images were recorded on a Bruker Dimension Icon using the ScanAssyst mode. A scanassyst-air canteliver was used with a spring constant of 0.4 N/m and a resonant frequency of 70 KHz. AFM images were acquired at a scan rate of 0.977 Hz applying a peak force of 1.2 nm over 10 μm with 512 samples per line.

Scanning Electron Microscopy (SEM) and Energy Dispersive X-ray (EDX)

All SEM images were recorded on a ZEISS 1550VP FESEM instrument, equipped with in-lens SE, below-lens SE, variable pressure SE and Robinson-type BSE detectors. EDX measurements were done on an Oxford X-Max SDD X-ray Energy Dispersive Spectrometer (EDS) system.

X-ray Diffraction (XRD)

The crystal structures were determined through XRD measurements using a Bruker DISCOVER D8 diffractometer with Cu Kα radiation from a Bruker ImS source (50 kV voltage and 1000 μA current). With a 0.3 mm collimator and 6° incident angle, a two theta scan mode was used and the effective thin film measurement foot print was approximately 3 mm. The grazing x-ray diffraction was measured using the same two theta scan mode but with a 0.1 mm collimator and 0.5° incident angle. Diffraction images were collected using a two-dimensional VÅNTEC-500 detector and integrated into one-dimensional patterns using DIFFRAC.SUITE™ EVA software.

Supporting Figures and Tables

Table S1. Faradaic efficiency (%) for CO_2RR products and hydrogen obtained during CO_2RR without and with 10 mM **1-Br$_2$** in a CO_2 saturated 0.1 M $KHCO_3$ electrolyte at -1.07 V.

Additive	Faradaic Efficiency (%)										j (mA/cm^2)
	Run	H_2	CO	HCOOH	CH_4	C_2H_4	C_2H_5OH	C_3H_7OH	C_2	Total	
-	1	36.4	1.1	3.4	22.0	15.8	8.2	3.2	29.7	92.6	-5.0
	2	49.4	2.9	2.7	14.0	11.1	7.6	2.7	25.2	97.1	-4.2
	3	42.5	2.6	2.6	24.7	10.1	5.9	2.6	23.0	96.6	-4.2
	Average	42.8	2.2	2.9	20.2	12.3	7.2	2.8	26.0	95.4	-4.5
1-Br$_2$	1	17.8	0.3	6.2	0.0	45.2	14.7	3.1	63.1	87.3	-3.9
	2	13.6	1.0	6.1	0.1	45.6	15.4	3.8	64.7	85.5	-3.5
	3	15.2	0.7	6.3	0.0	45.4	13.8	3.8	62.9	85.1	-3.8
	Average	15.5	0.7	6.2	0.1	45.4	14.6	3.6	63.6	86.0	-3.8

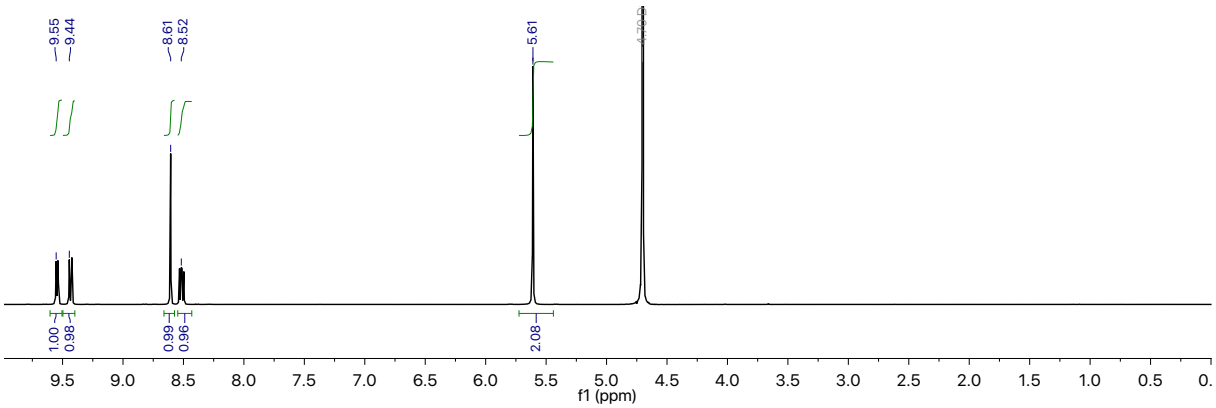

Figure S1. ^{1}H NMR spectrum of **1-Br$_2$** (D_2O, 298 K).

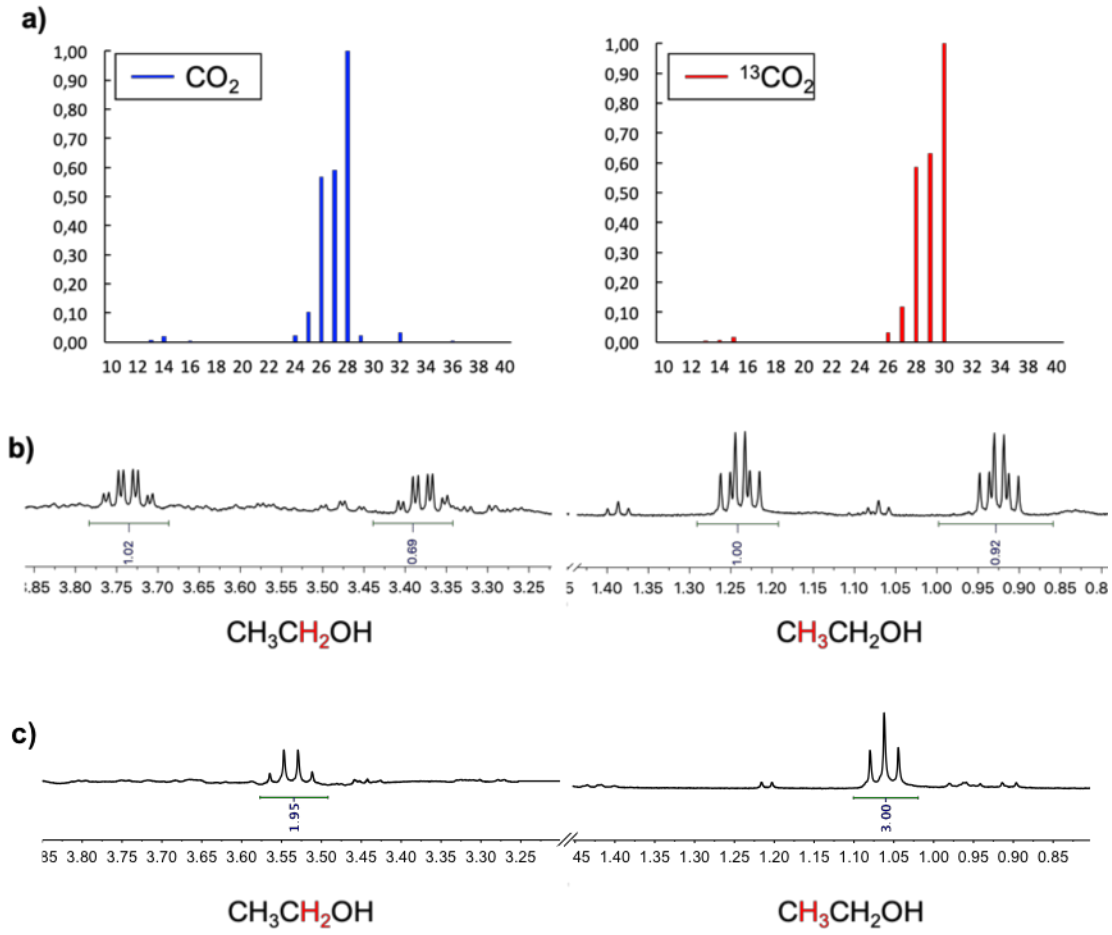

Figure S2. (a) GC-MS analyses of ethylene generated during CO_2RR at -1.07 V with 10 mM of **1-Br$_2$** with natural abundance (blue) and ^{13}C-enriched (red) CO_2-saturated $KHCO_3$ (0.1 M). ^{1}H NMR spectra (H_2O:D_2O = 9:1, 298 K) of ethanol produced under the same electrocatalytic conditions with ^{13}C-enriched CO_2 (b) and with natural abundance CO_2-saturated $KHCO_3$ (c).

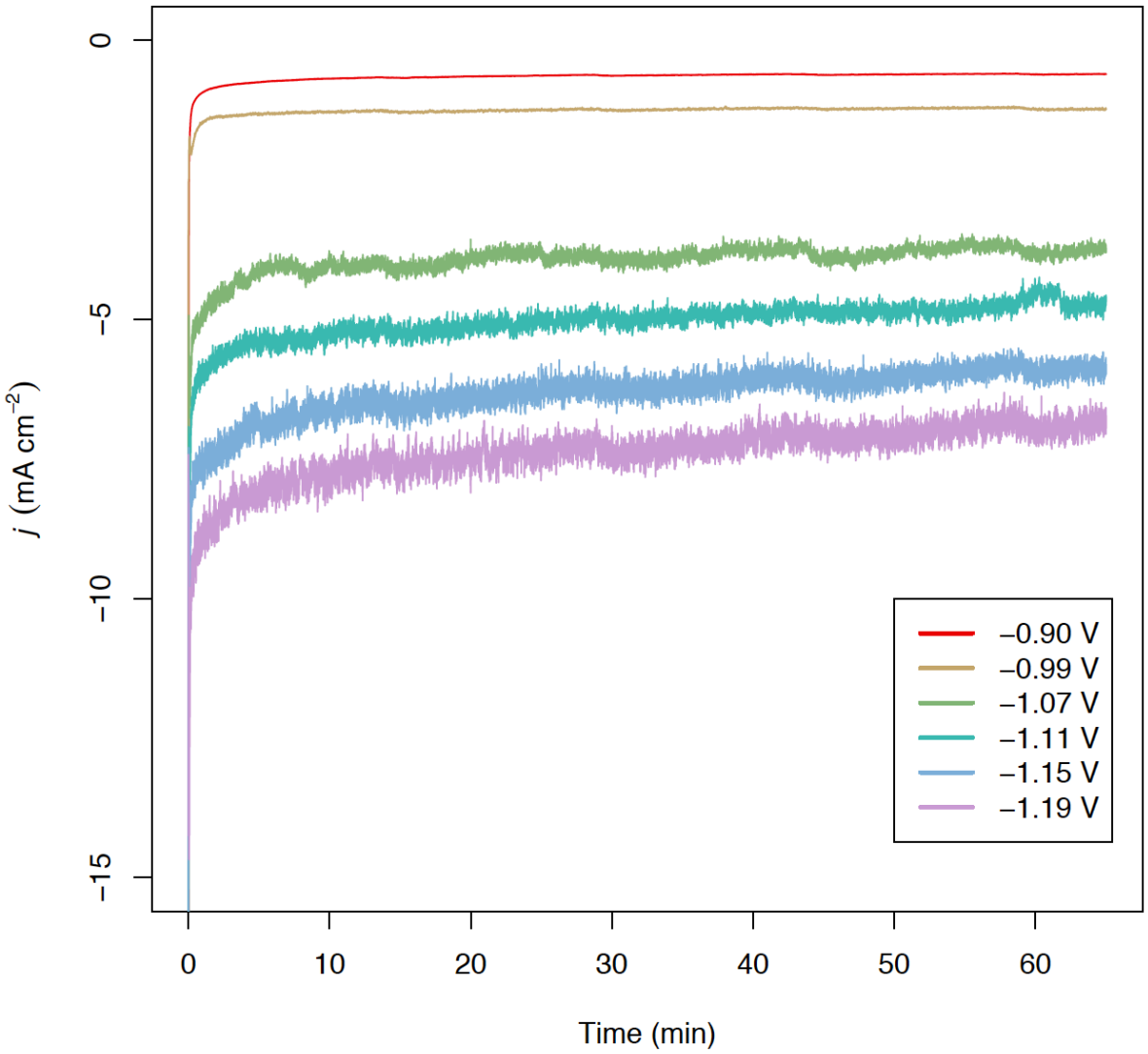

Figure S3. Chronoamperograms of electrolysis on a Cu electrode in a CO_2-saturated 0.1 M $KHCO_3$ electrolyte with 10 mM of **1-Br$_2$** at different potentials.

Table S2. Faradaic efficiencies for CO_2RR products and hydrogen obtained during catalytic runs in the presence of 10 mM **1-Br$_2$** at different potentials. The results are from the average of three runs.

Potential (V)	Faradaic Efficiency (%)									j (mA cm^{-2})
	H_2	CO	HCOOH	CH_4	C_2H_4	C_2H_5OH	C_3H_7OH	C_2	Total	
-1.19	40.5	0.2	0.1	0.8	28.0	19.0	1.2	48.2	90.7	-7.4
-1.15	25.2	0.4	1.5	0.4	39.7	20.7	1.8	62.2	89.8	-6.4
-1.11	19.1	0.6	2.5	0.3	44.0	17.9	2.0	64.0	86.5	-6.9
-1.07	15.5	0.7	6.2	0.1	45.4	14.6	3.6	63.6	86.0	-3.8
-0.99	21.6	4.7	21.8	n.d.	26.9	n.d.	n.d.	26.9	75.0	-1.6
-0.90	22.3	14.9	35.1	n.d.	11.0	n.d.	n.d.	11.0	83.2	-0.6

Table S3. Faradaic efficiency (%) for CO_2RR products and hydrogen obtained at -1.07 V using different concentration of **1-Br$_2$**.

Concentration	Faradaic Efficiency (%)									j (mA cm^{-2})
	H_2	CO	HCOOH	CH_4	C_2H_4	C_2H_5OH	C_3H_7OH	C_2	Total	
10 mM	15.5	0.7	6.2	0.1	45.4	14.6	3.6	63.6	86.0	-3.8
1 mM	25.0	1.1	5.9	0.1	41.6	16.5	8.1	66.2	97.2	-3.2
0.1 mM	28.9	0.8	7.4	0.4	34.3	13.8	6.3	54.4	91.9	-3.7

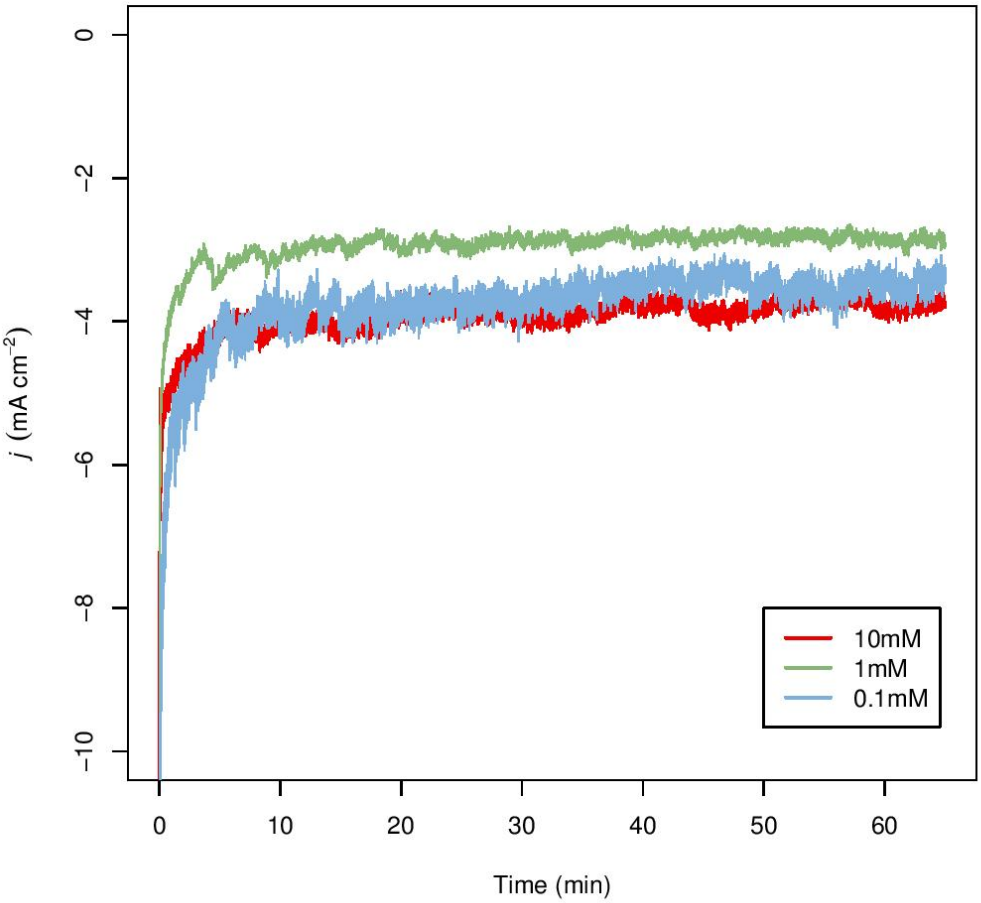

Figure S4. Chronoamperograms of electrolysis on a Cu electrode in a CO_2-saturated 0.1 M $KHCO_3$ electrolyte with different concentrations of **1-Br$_2$** at -1.07 V.

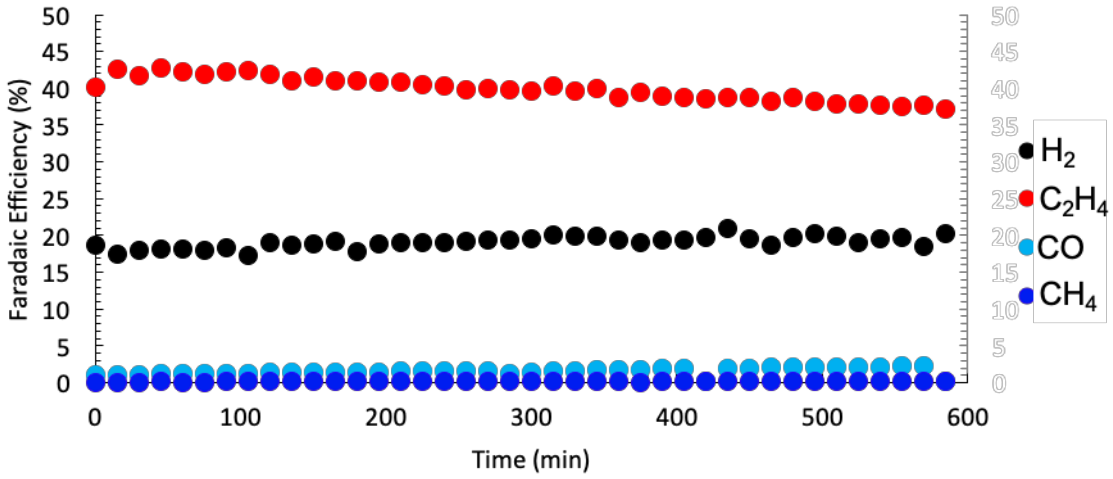

Figure S5. Plot of the Faradaic efficiencies for gaseous products over 10 h on a Cu electrode in a CO_2-saturated 0.1 M $KHCO_3$ electrolyte with 10 mM of **1-Br$_2$** at -1.07 V.

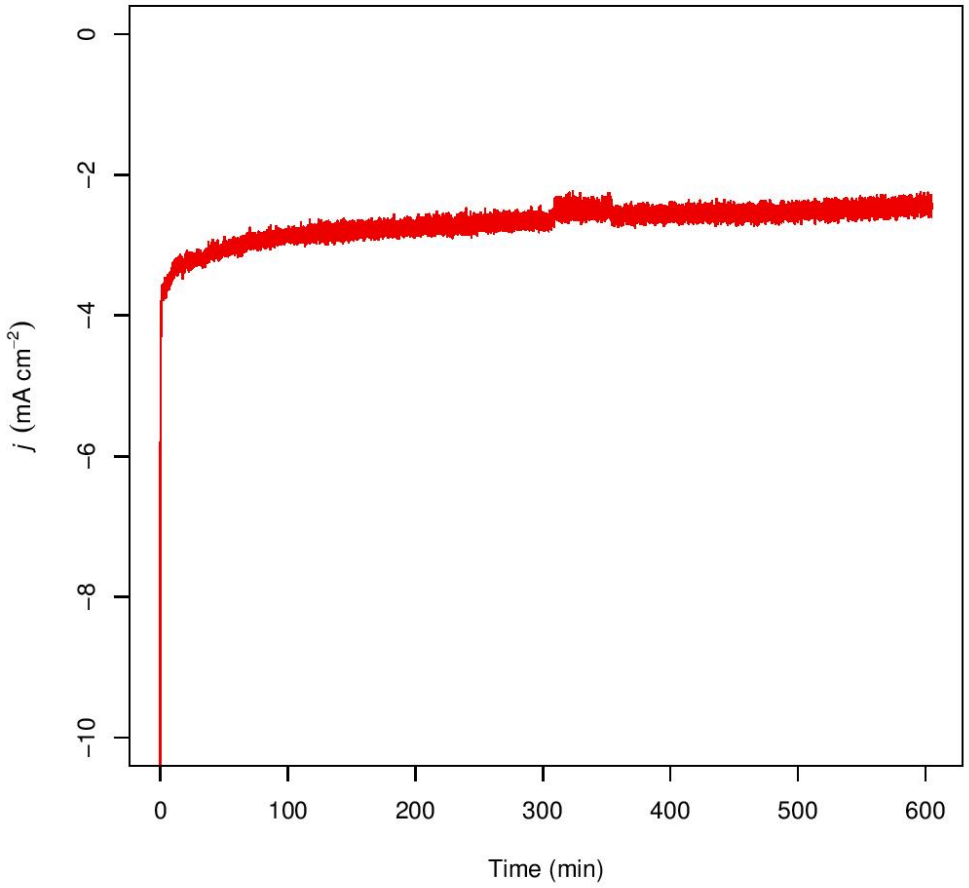

Figure S6. Chronoamperograms of electrolysis on a Cu electrode in a CO_2-saturated 0.1 M $KHCO_3$ electrolyte with 10 mM of **1-Br$_2$** for 10 h.

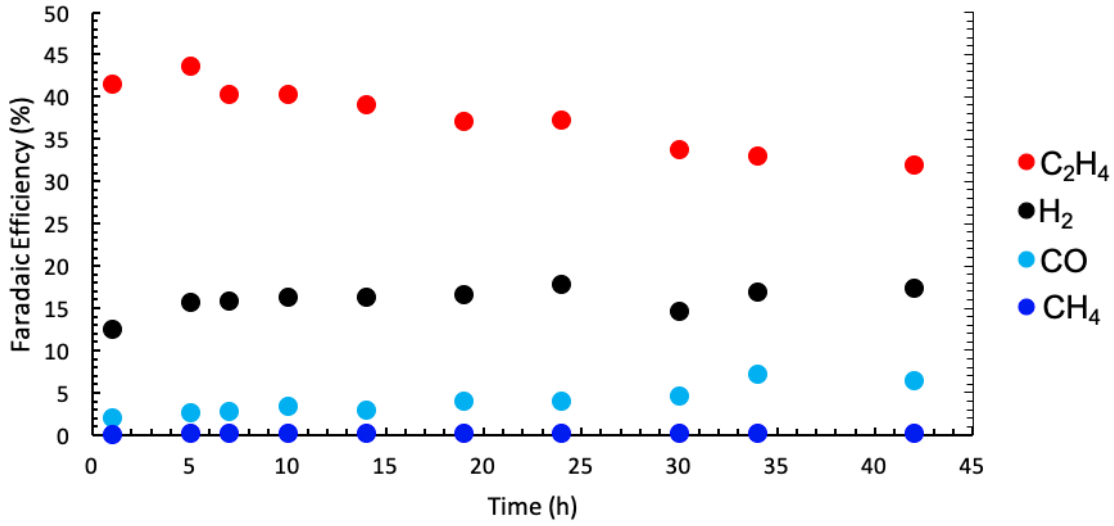

Figure S7. Plot of the faradaic efficiencies for gaseous products over 42h on a Cu electrode in a CO_2-saturated 0.1 M $KHCO_3$ electrolyte with 10 mM of **1-Br$_2$** at -1.07 V.

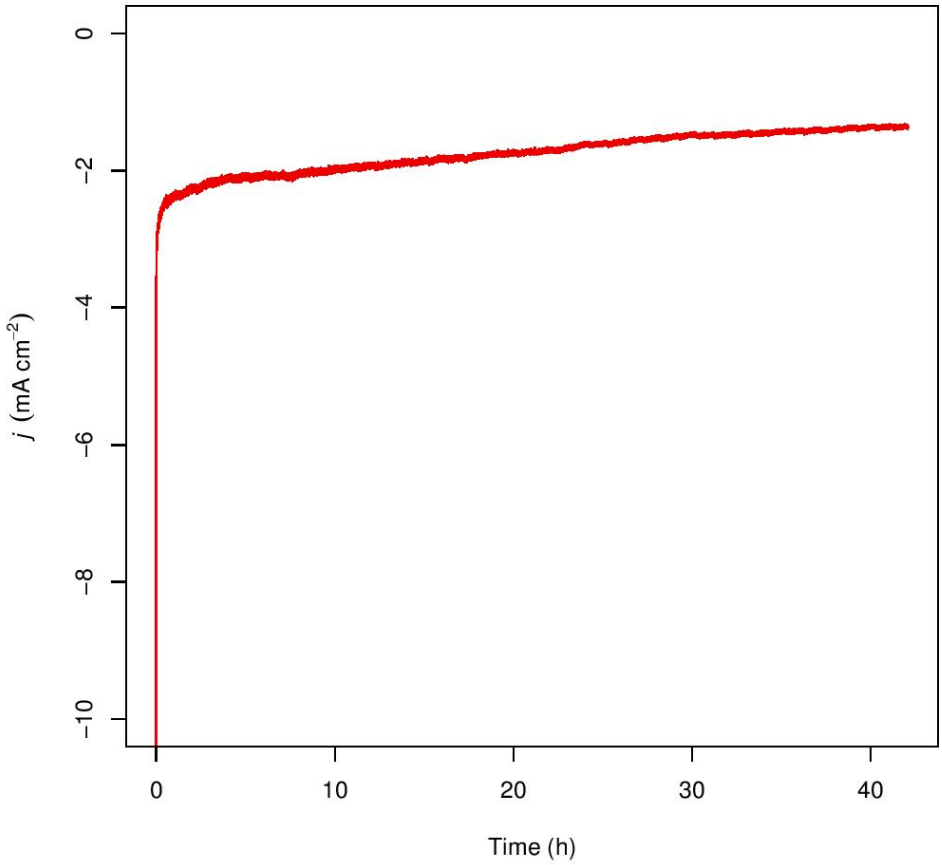

Figure S8. Chronoamperograms of electrolysis on a Cu electrode in a CO_2 saturated 0.1 M $KHCO_3$ electrolyte with 10 mM of **1-Br$_2$** for 42 h.

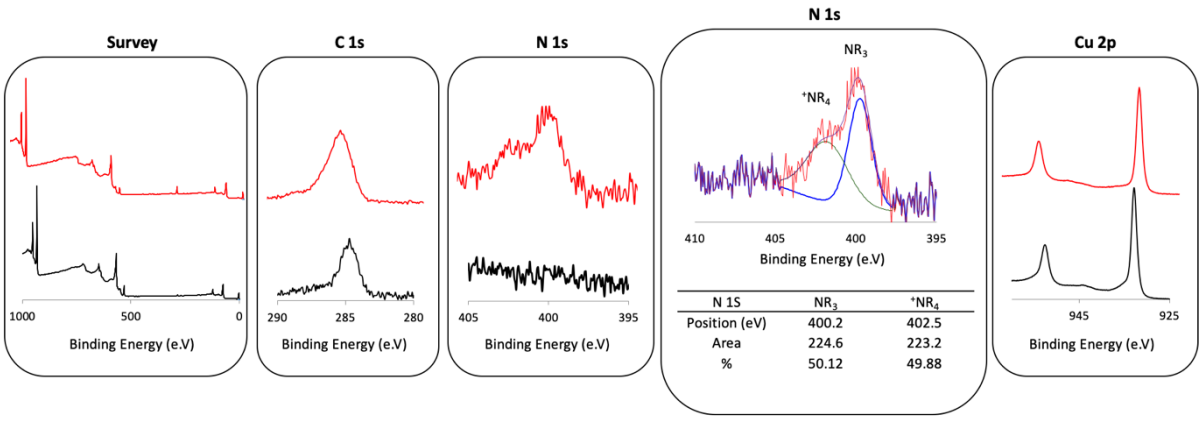

Figure S9. (a) Normalized X-ray photoelectron spectra of Cu electrodes after electrolysis at -1.07 V in $KHCO_3$ (0.1 M) with (red trace) and without (black trace) **1-Br$_2$** (10 mM). The broad N 1s peak has been deconvoluted into two peaks corresponding to quaternary amine (green trace) and tertiary amine (blue trace) nitrogens. The purple trace corresponds to the overall fitting of the model. XPS spectra suggest that the surfaces of copper foils are mixtures of copper metal and Cu_2O after electrolysis both with and without 10 mM of **1-Br$_2$**. Due to the complexity of the organic molecule in the C 1s region, spectral energy for all samples are calibrated using the Cu 2p3/2 peak (932.63 eV) instead of C 1s. The Cu 2p band for the two samples shows a pair of 2p 3/2 and 2p1/2 peaks, indicative of Cu metal and/or Cu_2O. These two oxidation states in the 2p region give near identical binding energy. The lack of large satellites at 940–945 and 960–963 eV indicates that the surfaces do not contain CuO. For the sample after electrolysis in the presence of **1-Br$_2$**, two N 1s peaks are observed at 400.2 eV and 402.5 eV, which correspond to a tertiary amine and a quaternary amine nitrogen, respectively.[8,9] Integration of the two peaks indicates a 50% ratio of the two different types of nitrogen present in the organic film. These observations are consistent with the ^{1}H NMR spectrum assignment of the two dimers ***ortho-ortho*** **(1-Br)$_2$** and ***para-para*** **(1-Br)$_2$**.

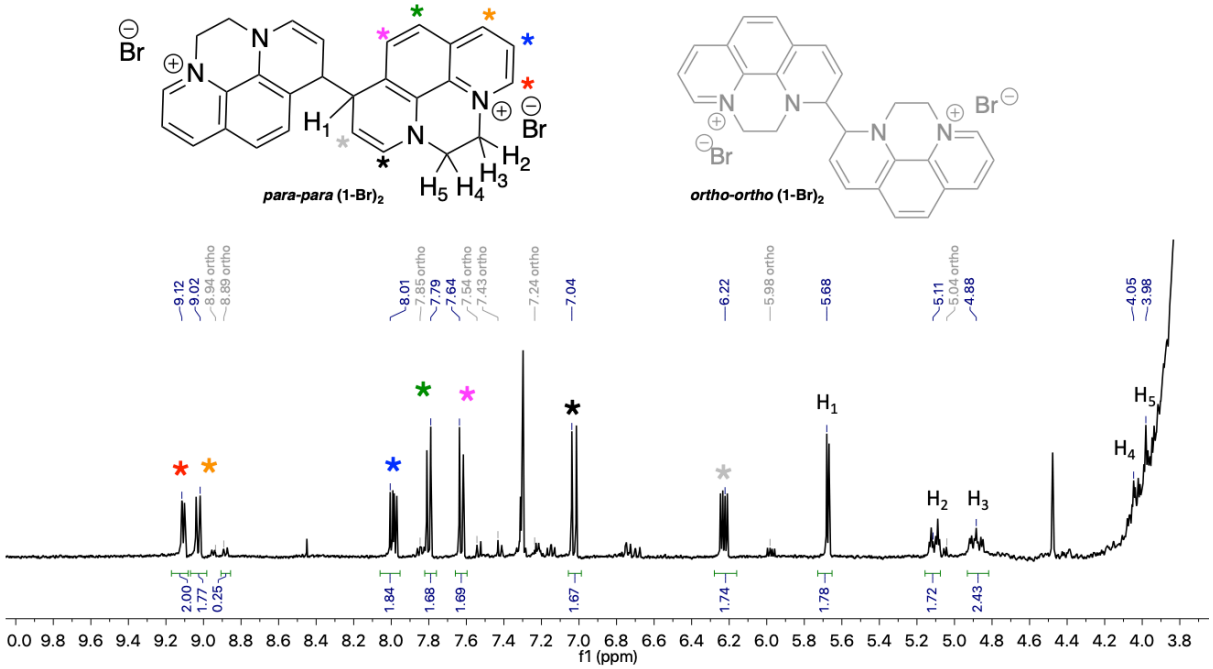

Figure S10. Proposed structure of the dimers (top), ***para-para*** **(1-Br)$_2$** and ***ortho-ortho*** **(1-Br)$_2$** (black and grey, respectively). ^{1}H NMR spectrum (bottom, DMSO-d$_6$, 298 K) of the organic film extracted from a post catalysis Cu electrode at -1.4 V in a CO_2 saturated 0.1 M $KHCO_3$ electrolyte with 10 mM of **1-Br$_2$**. The ^{1}H NMR spectrum suggests the formation of two products which have been assigned to the *para-para* and the *ortho-ortho* coupling of two phenanthrolinium radicals (blue and grey labels, respectively). The *para-para* product is the major species (88 %). Two resonances from the bridge overlap with the water peak. Nevertheless, COSY shows the coupling of these two resonances with the resonances at 5.11 ppm and 4.88 ppm, corresponding to the two other protons of the bridge. The ***para-para*** **(1-Br)$_2$** and ***ortho-ortho*** **(1-Br)$_2$** products represent > 95% of the material present on the surface of the electrode. Some minor resonances at 8.50 ppm (s), 7.30 (s), 7.18 ppm (m), 6.75 ppm (m) and 6.65 ppm (m) could not be assigned. They could come from unidentified by-products or other isomers of **(1-Br)$_2$**.

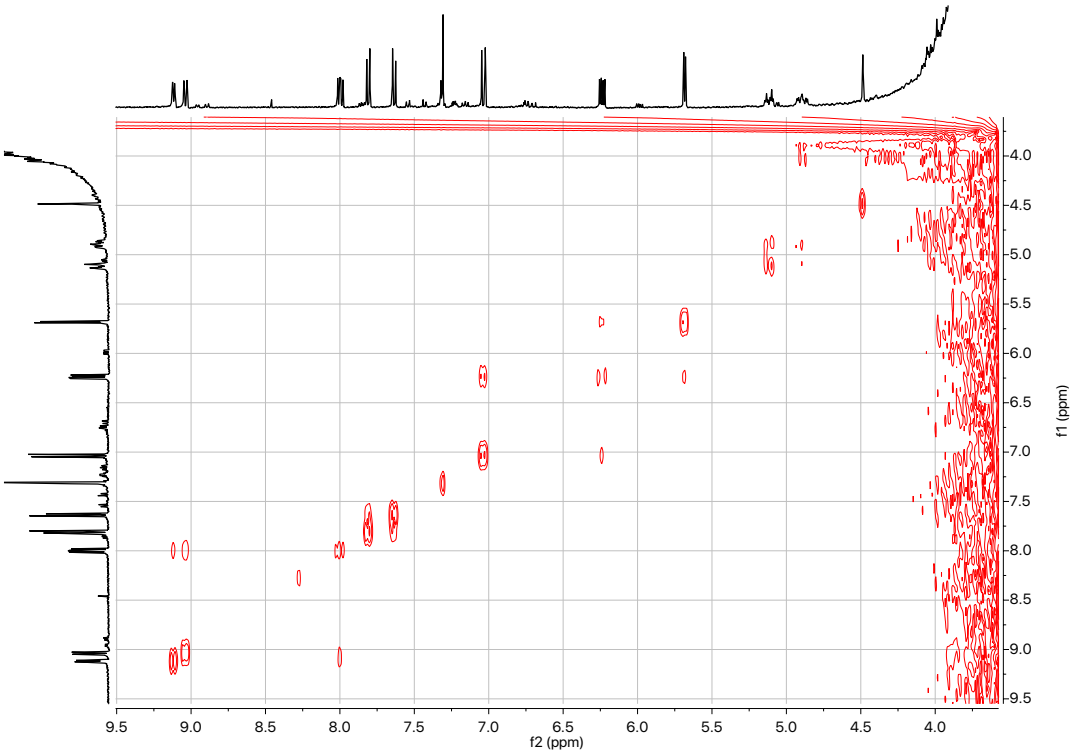

Figure S11. ^{1}H-^{1}H COSY spectrum of the organic film extracted from a post catalysis Cu electrode at -1.4 V in a CO_2 saturated 0.1 M $KHCO_3$ electrolyte with 10 mM of **1-Br$_2$**. (DMSO-d$_6$, 298 K).

Table S4. Faradaic efficiency (%) towards different CO_2RR products during recycling experiments in a CO_2 saturated 0.1 M $KHCO_3$ electrolyte at -1.07 V.[a]

Run	Faradaic Efficiency (%)									j (mA cm^{-2})
	H_2	CO	HCOOH	CH_4	C_2H_4	C_2H_5OH	C_3H_7OH	C_2	Total	
1*	23.1	1.0	8.4	0.3	38.2	15.3	3.8	57.3	90.1	-3.8
2**	32.0	0.7	9.7	0.4	36.5	14.9	3.5	54.9	97.7	-3.4
3***	27.5	1.7	9.6	2.9	38.4	15.4	3.7	57.5	99.2	-4.2

*10 h reaction; **1 h reaction; ***3 h reaction.

[a] Before the first run, the Cu electrode was functionalized with a thick layer of the organic film. This was done by performing electrocatalysis at -1.4 V for 1h in 0.1 M $KHCO_3$ in presence of 10 mM of **1-Br$_2$**. The cell was then cleaned and the functionalized electrode was rinsed gently with water to remove the solution but avoid mechanically disturbing the insoluble film. All the runs were performed using the same functionalized Cu electrode. The cell was cleaned between each run and the electrode was washed gently with water and kept in air. Fresh 0.1 M $KHCO_3$ electrolyte was used for each run (no additive).

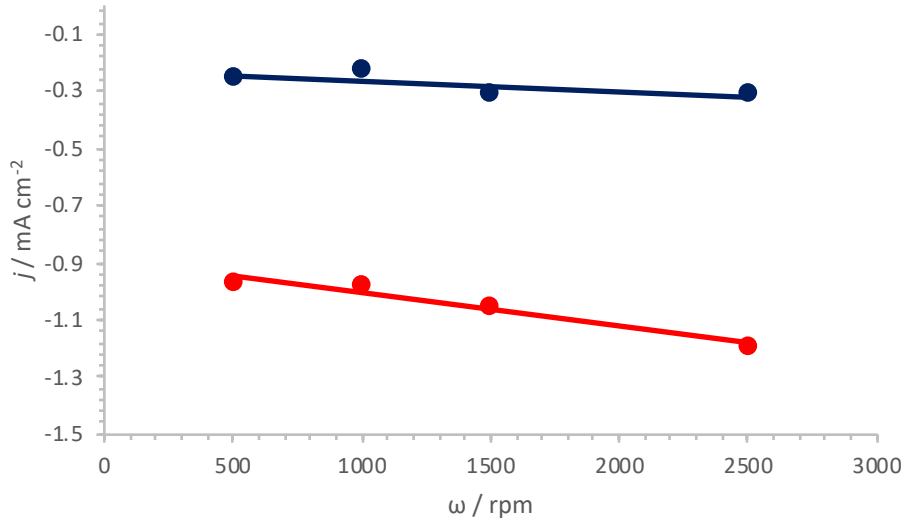

Figure S12. Catalytic currents as a function of rotation rate of a Cu rotating disk electrode in Ar-saturated 0.1 M $KHCO_3$ at -1.10 V vs RHE in the absence (red trace) and in the presence of 10 mM of **1-Br$_2$** (blue trace). Lines are included as guides to the eye.

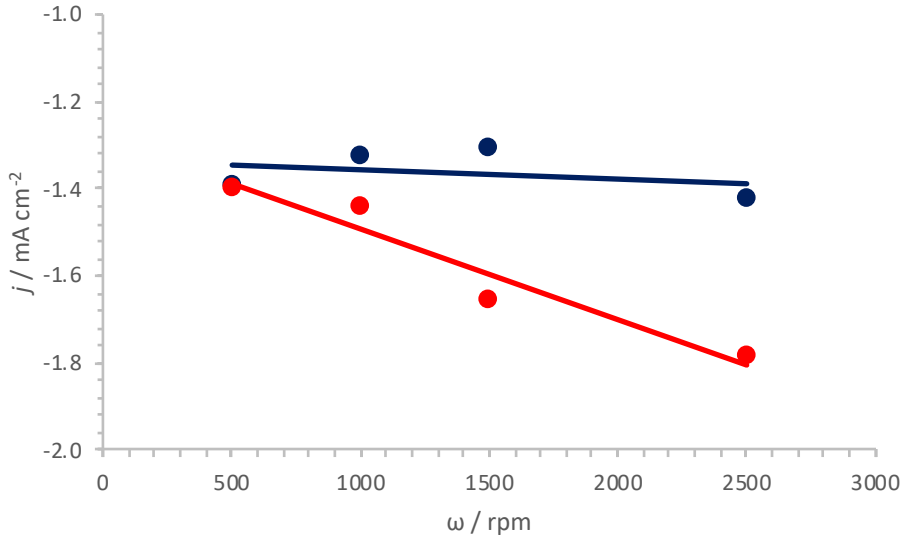

Figure 13. Catalytic currents as a function of rotation rate of a Cu rotating disk electrode in CO_2-saturated 0.1 M $KHCO_3$ at -1.10 V vs RHE in the absence (red trace) and in the presence of 10 mM of **1-Br$_2$** (blue trace). Lines are included as guides to the eye.

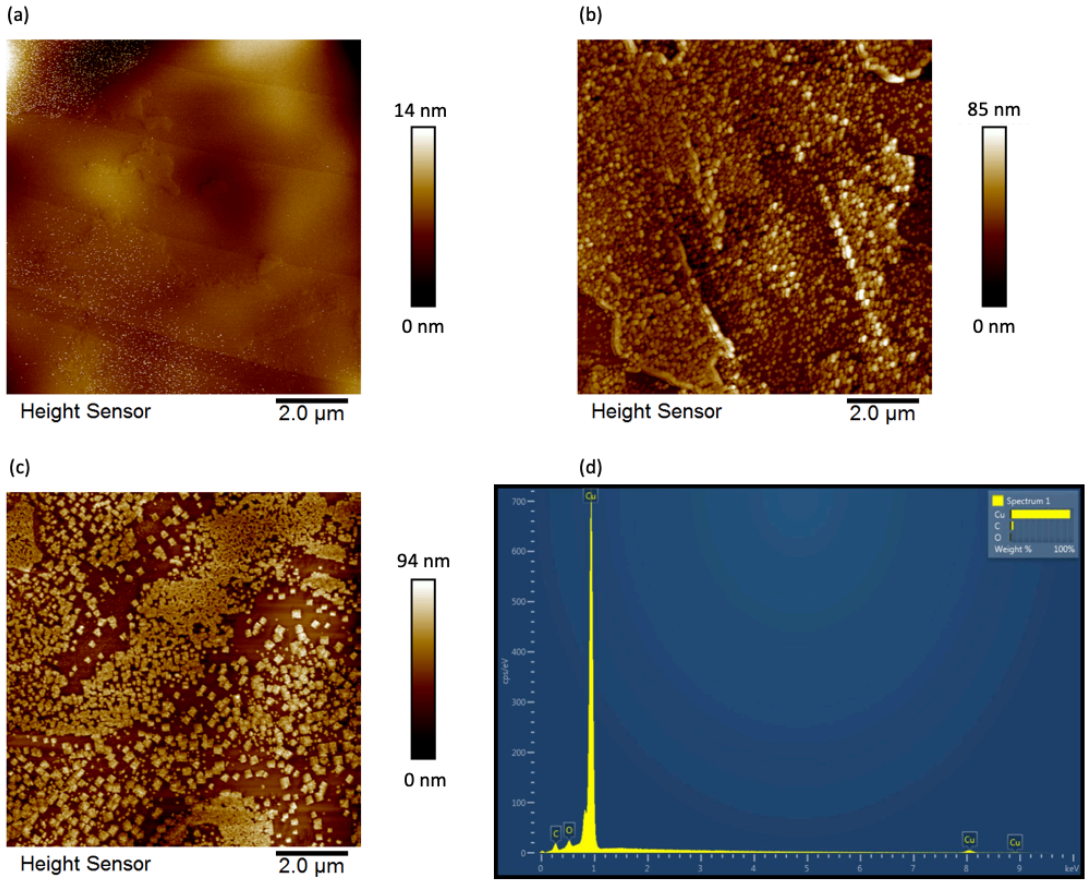

Figure S14. Ex-situ AFM images of Cu electrodes after electropolishing (a); after 65 min of electrocatalysis at -1.07 V in a CO_2-saturated 0.1 M $KHCO_3$ without additives (b); with 10 mM of **1-Br$_2$** (c). (d) EDX spectrum of the surface of (c).

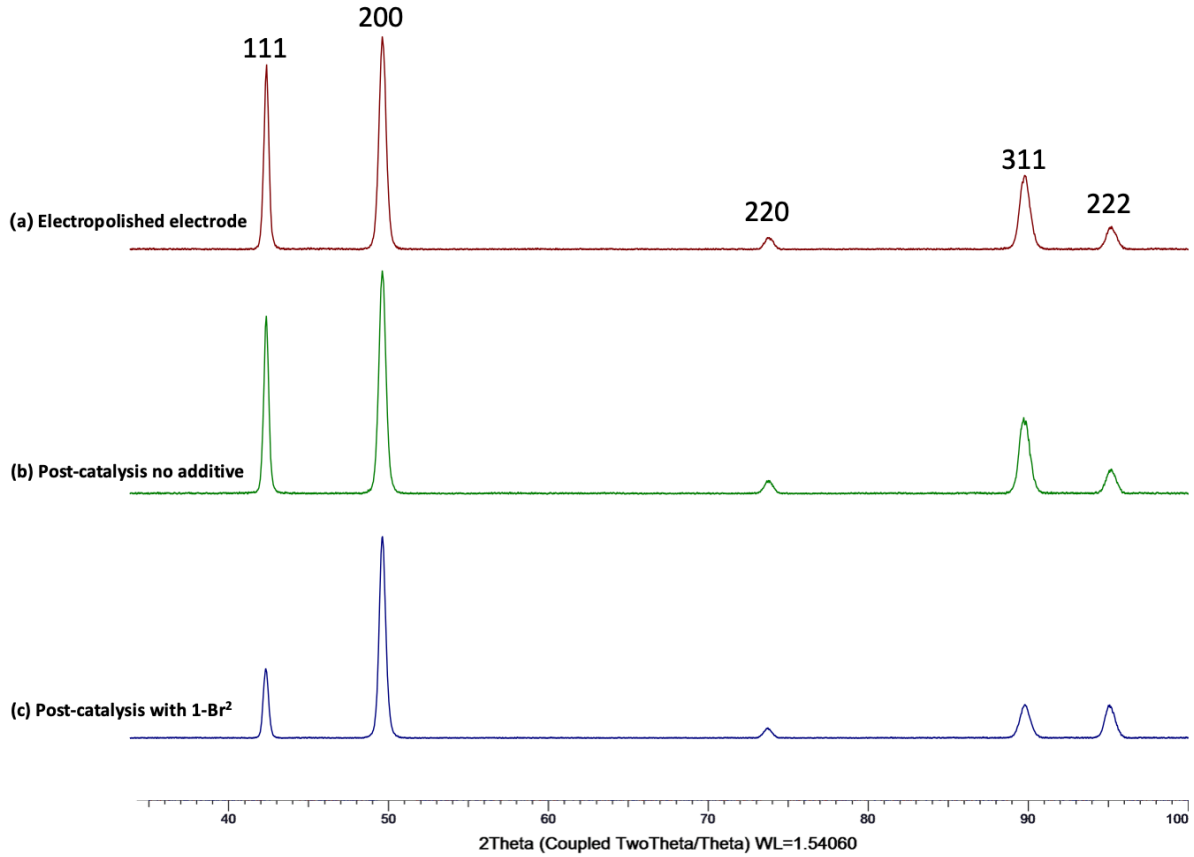

Figure S15. Typical normalized XRD pattern of (a) an electropolished Cu electrode; post catalysis Cu electrodes (b) without additive; (c) with **1-Br$_2$**.

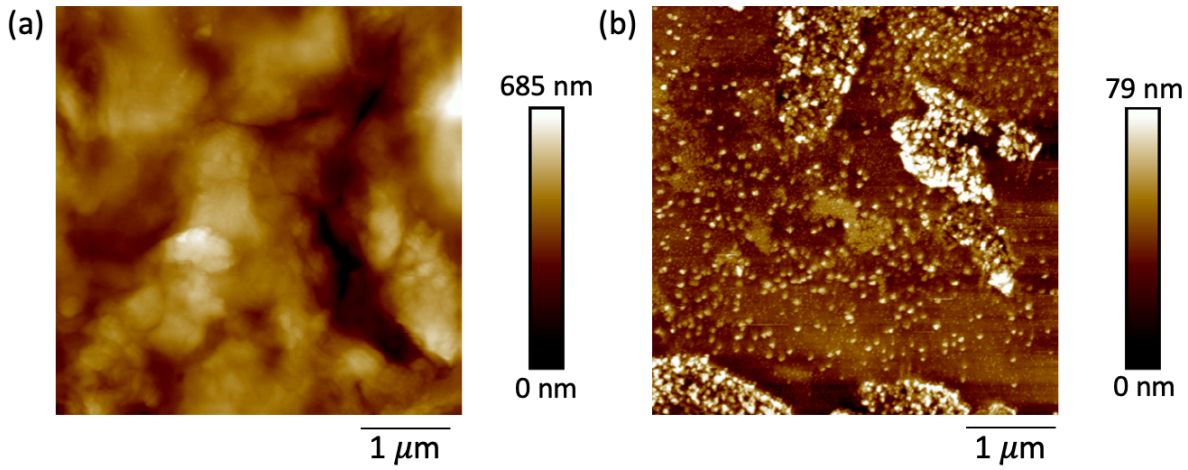

Figure S16. Ex-situ AFM images of the same post catalysis Cu electrode after 43 h of electroreduction at -1.07 V (a) before and (b) after the extraction of the organic film.

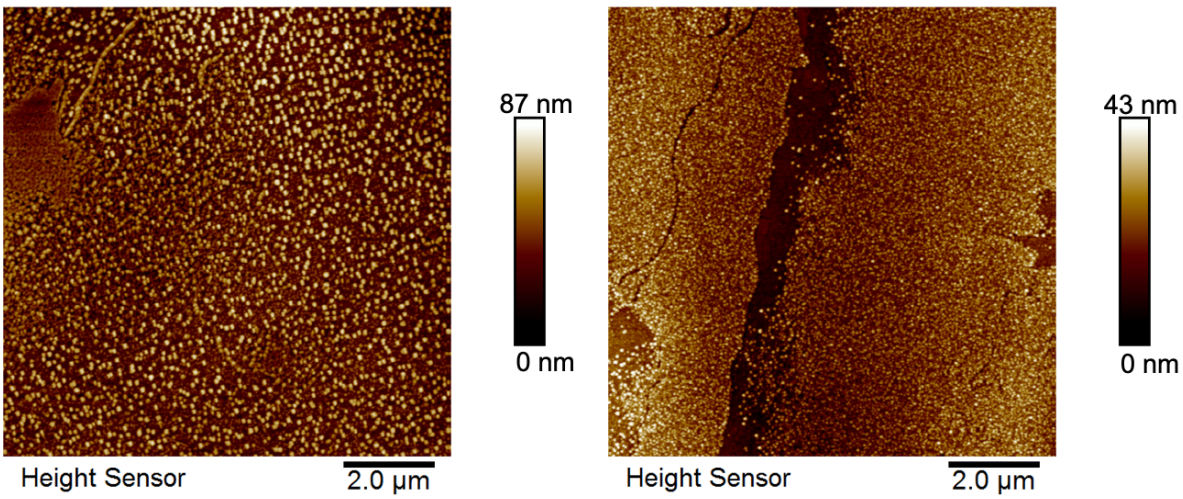

Figure S17. Ex-situ AFM images a) after three cycles of PEIS; and b) after 65 min of electrocatalysis at -1.07 V in presence of 20 mM of KBr.

Table S5. Faradaic efficiency (%) for CO_2RR products and hydrogen obtained during catalytic runs in a CO_2-saturated 0.1 M $KHCO_3$ electrolyte at -1.07 V with 20 mM of KBr.

Additive	Faradaic Efficiency (%)										j (mA cm^{-2})
	Run	H_2	CO	HCOOH	CH_4	C_2H_4	C_2H_5OH	C_3H_7OH	C_2	Total	
KBr	1	55.7	1.1	8.0	19.7	8.2	3.8	3.1	15.1	99.6	-5.3
KBr	2	47.5	1.8	17.4	15.8	11.5	3.9	3.1	18.5	101.6	-5.8
	Average	51.6	1.5	12.9	17.7	9.8	3.8	3.1	16.8	100.6	-5.5

Table S6. Faradaic efficiency (%) for CO_2RR products and hydrogen obtained during catalytic runs in a CO_2 saturated 0.1 M $KHCO_3$ electrolyte at -1.07 V with 10 mM **1-X$_2$** (X = Br^-, Cl^-, OTf^- or I^-).

Additive	Faradaic Efficiency (%)										j (mA cm^{-2})
	Run	H_2	CO	HCOOH	CH_4	C_2H_4	C_2H_5OH	C_3H_7OH	C_2	Total	
1-Br$_2$	Average	15.5	0.7	6.2	0.1	45.4	14.6	3.6	63.6	86.0	-3.8
1-(OTf)$_2$	1	26.7	2.0	13.9	0.2	36.4	15.2	5.2	56.8	99.7	-2.4
	2	21.5	1.2	13.9	0.1	38.4	12.9	4.7	56.0	92.7	-2.5
	Average	24.1	1.6	13.9	0.1	37.4	14.1	4.9	56.4	96.2	-2.4
1-Cl$_2$	1	23.6	1.1	20.0	0.1	35.0	7.5	4.0	46.5	91.0	-2.5
	2	27.6	1.9	21.2	0.2	32.7	9.3	6.8	48.5	99.6	-2.4
	Average	25.6	1.5	20.6	0.1	33.8	8.4	5.4	47.5	95.3	-2.4
1-I$_2$	1	18.9	1.3	13.0	0.1	42.5	12.3	3.3	58.1	91.2	-2.6
	2	23.8	2.2	13.9	0.1	41.5	12.9	4.7	59.1	99.0	-2.5
	Average	21.4	1.7	13.4	0.1	42.0	12.6	4.0	58.6	95.1	-2.5

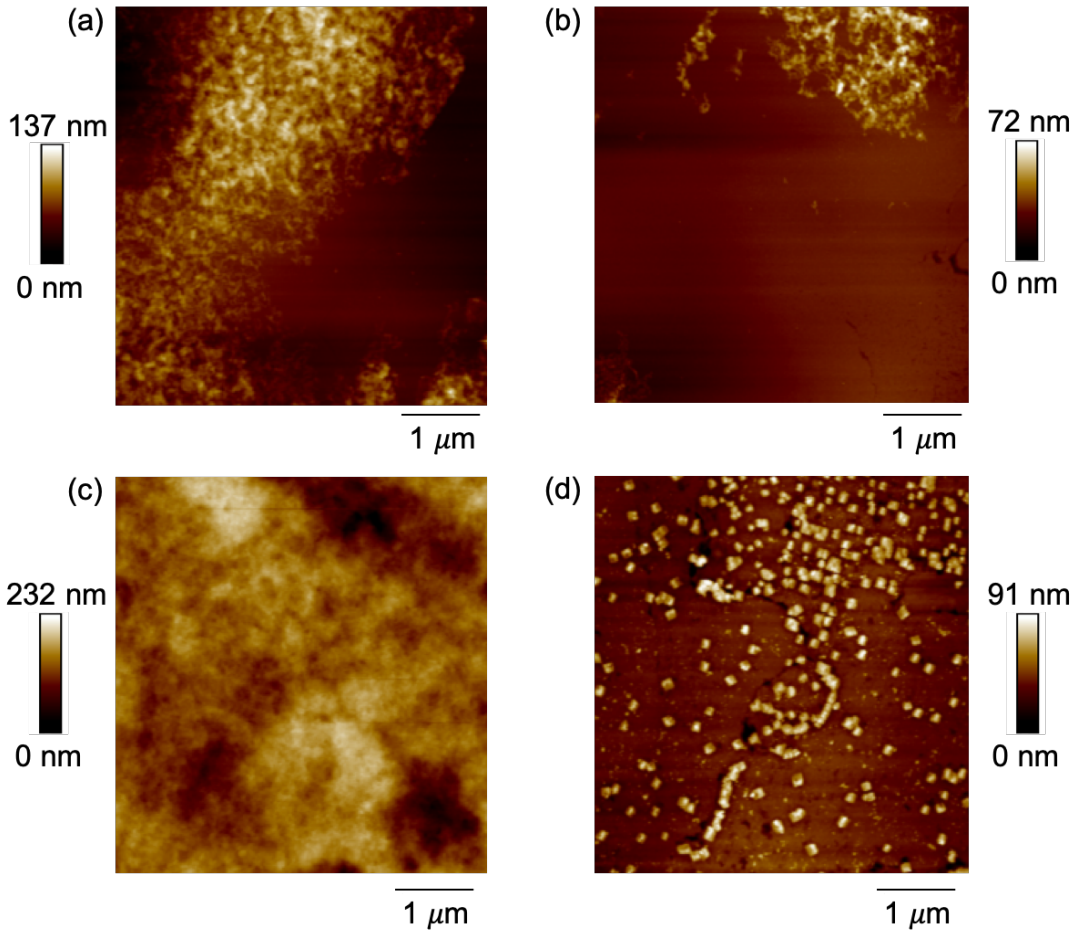

Figure S18. *Ex-situ* AFM images of Cu electrodes after 65 min of electrocatalysis at -1.07 V in 0.1 M $KHCO_3$ with (a) **1-Cl$_2$**; (b) **1-(OTf)$_2$**; (c) **1-I$_2$**; (d) **1-I$_2$** after extracting the organic film.

Table S7. Faradaic efficiency (%) for CO_2RR products and hydrogen obtained during a catalytic run in a CO_2-saturated 0.1 M $KHCO_3$ electrolyte at -1.07 V in the presence of **1-Br$_2$** (run 1); after removing the electrodeposited film and resubmitting the same electrode with no additive in the electrolyte (run 2).

Additive	Faradaic Efficiency (%)										j (mA.cm^{-2})
	Run	H_2	CO	HCOOH	CH_4	C_2H_4	C_2H_5OH	C_3H_7OH	C_2	Total	
1-Br$_2$	1	12.2	1.8	6.2	0.1	44	14.6	3,6	62.1	82.2	-3.2
-	2	59.6	0.6	11.3	9.4	10.2	5.0	4.4	19.6	97.8	-3.7

Table S8. Faradaic efficiency (%) for CO_2RR products and hydrogen obtained during a catalytic run in a CO_2-saturated 0.1 M $KHCO_3$ electrolyte at -1.07 V with **1-Br$_2$** (run 1); without additive in the electrolyte and using the resulting electrode from run 1 (run 2).

Additive	Faradaic Efficiency (%)										j (mA cm^{-2})
	Run	H_2	CO	HCOOH	CH_4	C_2H_4	C_2H_5OH	C_3H_7OH	C_2	Total	
1-Br$_2$	1	12.2	1.8	6.2	0.1	44	14.6	3,6	62.1	82.23	-3.2
-	2	20.1	2.3	10.4	0.1	40	14.4	3.2	57.7	90.5	-3.8

Dimerization Mechanism

Intrigued by the formation of the *para-para* and *ortho-ortho* dimers resulting from the electroreduction of **1-Br$_2$** by a polycrystalline copper electrode, the reduction of **1-Br$_2$** was investigated by cyclic voltammetry (CV) using a Cu disk as the working electrode and a platinum wire as the counter electrode (Figure S15). Under a CO_2 atmosphere, two irreversible reductive waves at −0.1 V and −0.4 V are present in the first scan and disappear completely in the second scan. This suggests that the electrode is insulated from the electrolyte by the organic film. The same ratio of *ortho-ortho and para-para* dimers is present as that observed via extraction of the copper electrode after a bulk electrolysis experiment, as described in the main text. In the present instance, the mixture of dimers can be observed by dissolving and analyzing by ^{1}H NMR spectrum of the film deposited on the electrode during the CV experiments (Figure S16). This indicates that film formation occurs in the initial stages of the electrocatalysis. Another chronoamperometry experiment was performed on a copper working electrode with a carbon rod counter electrode for 1 h under an N_2 atmosphere using a deuterated electrolyte and with 30 mM of **1-Br$_2$**. The solution rapidly changes color from pale yellow to deep red upon applying a potential of -1.07 V, characteristic of the formation of a phenanthrolinium radical (Figure S17). After 1 h of reaction time, both films formed on the Cu and the carbon rod electrode were dissolved in DMSO-d_6 to be analyzed, together with analysis of the electrolyte by ^{1}H NMR spectroscopy (Figure S18). The *ortho-ortho* and *para-para* dimers are the only products observable on the Cu surface. These products are not detected in the electrolyte, or from attempted extraction of the carbon rod. In the electrolyte, mainly the starting phenanthrolinium additive **1-Br$_2$** is observed after 1 h reaction time. Other side products are also observed in the electrolyte and via extraction of the carbon rod, which may be oligomeric/polymeric species that result from multiple couplings of phenanthrolinium radicals. When the same CV or chronoamperometry experiments is repeated using a glassy carbon rod as the working electrode, the *ortho-ortho* and *para-para* dimers are not detected on the surface of the electrode after extracting with DMSO-d_6 and analyzing the solution by ^{1}H NMR spectroscopy (Figure S19). Notably, when the one-electron reduced radical 1•-Br is generated in solution using zinc dust as a chemical reductant, dimerization is not observed. All of these observations lead to the conclusion that the dimerization process of the one-electron reduced form of **1-Br$_2$** is facilitated by the copper electrode surface.

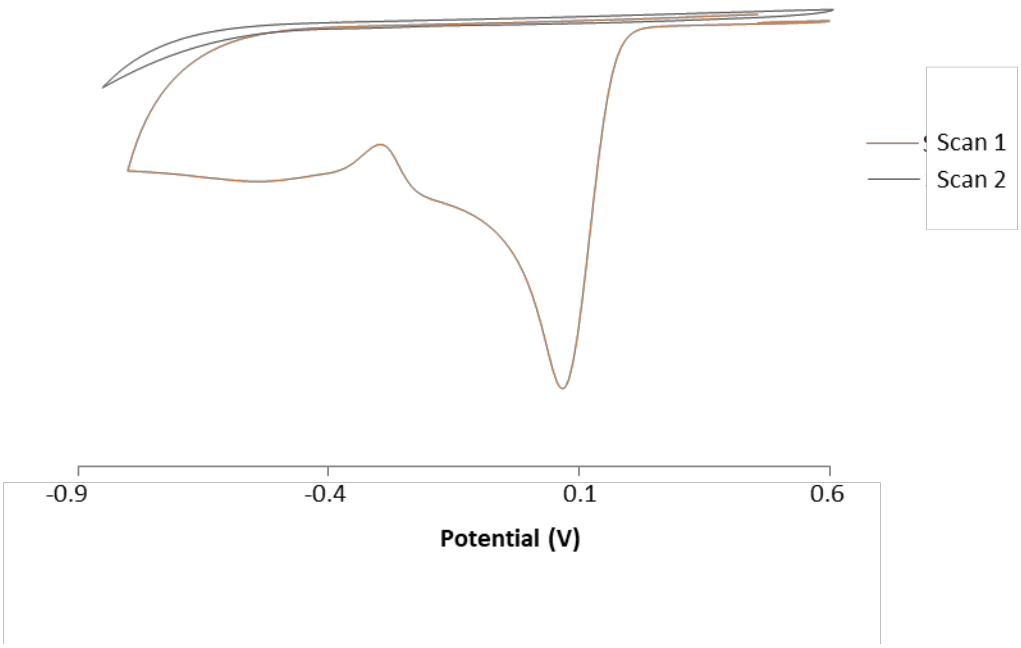

Figure S19. First and second scan cyclic voltammogramms of 10 mM **1-Br$_2$** under CO_2 with a Cu disk electrode in 0.1 M $KHCO_3$ electrolyte at a scan rate of 50 mV/s. Similar results are obtained under N_2

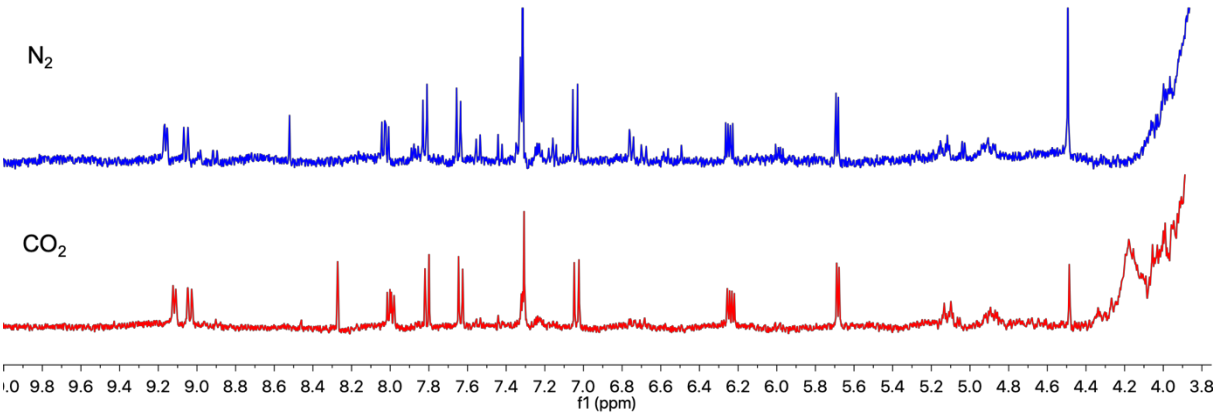

Figure S20. ^{1}H NMR (DMSO-d_6, 298 K) of the extracted films obtained after CV experiments under N_2 (top spectrum in blue) and CO_2 (bottom spectrum in red).

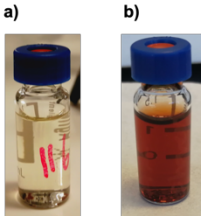

Figure S21. Photographs of the electrolyte containing 10 mM of **1-Br$_2$** in 0.1 M $KHCO_3$ a) before catalysis and b) just after catalysis.

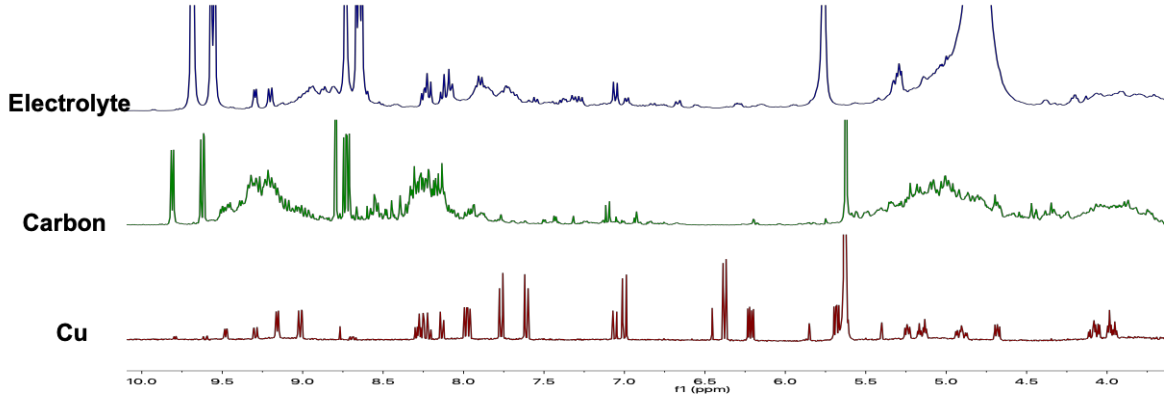

Figure S22. Stack of ^{1}H NMR spectra (298 K). The top trace corresponds to the electrolyte (D_2O), the middle trace to the organic precipitate extracted from the counter electrode (DMSO-d_6), and the bottom trace to the organic film extracted from the Cu electrode (DMSO-d_6).

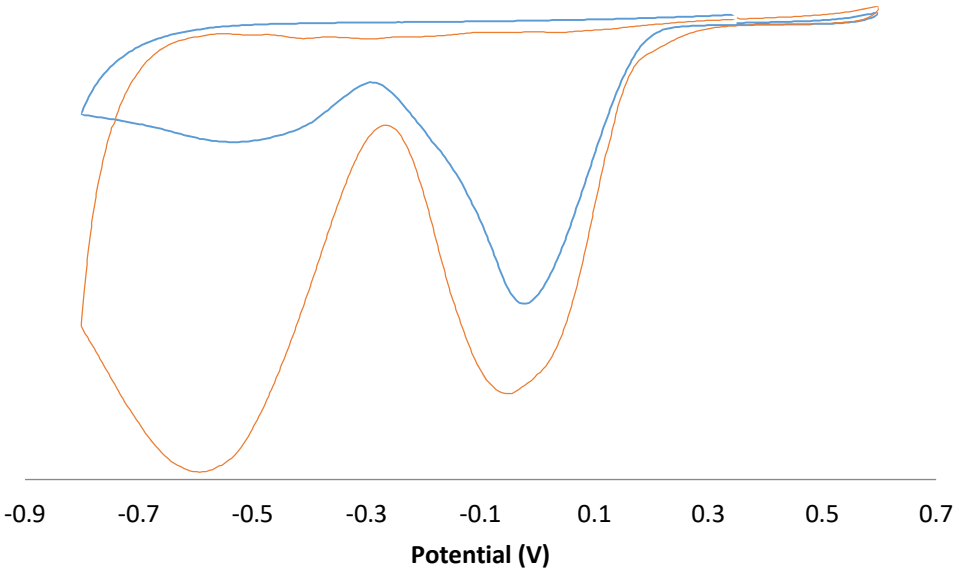

Figure S23. Cyclic voltammogramms on a glassy carbon electrode of 10 mM **1-Br$_2$**, in a CO_2-saturated 0.1 M $KHCO_3$ electrolyte at a scan rate of 50 mV/s between -0.9 V and 0.7 V of the first scan (blue curve) and the second scan (orange curve).

Reactivity studies of 1˙-Br with CO_2

Pyridinium radicals have been proposed to play a crucial role in the selectivity shift during CO_2RR by reacting with CO_2 to form a carbamate intermediate.[10–13] To rule out the possibility of a direct interaction between the molecule of CO_2 and the one-electron reduced species of **1-Br$_2$** without the involvement of Cu, the reactivity of **1˙-Br** was studied by EPR and UV-VIS spectroscopy (Figures S20-22). Upon addition of an excess of Zn dust to a 10 mM aqueous solution of **1˙-Br** under N_2 atmosphere, a rapid change in color to deep red was observed, characteristic of the formation of radical **1˙-Br**, as previously reported.[1,2] Then, the solution was treated with CO_2 and the corresponding EPR and UV-VIS spectra were recorded. No differences in the spectra were observed before and after the addition of carbon dioxide, suggesting that radical **1˙-Br** does not react with CO_2 and thus, such a species is not involved directly in the CO_2RR mechanism.

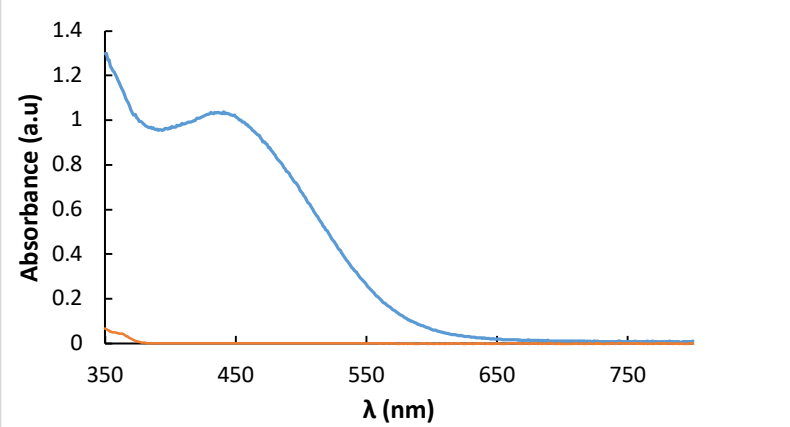

Figure S24. Visible spectra of **1-Br$_2$** (orange) and **1˙-Br** (blue) in water.

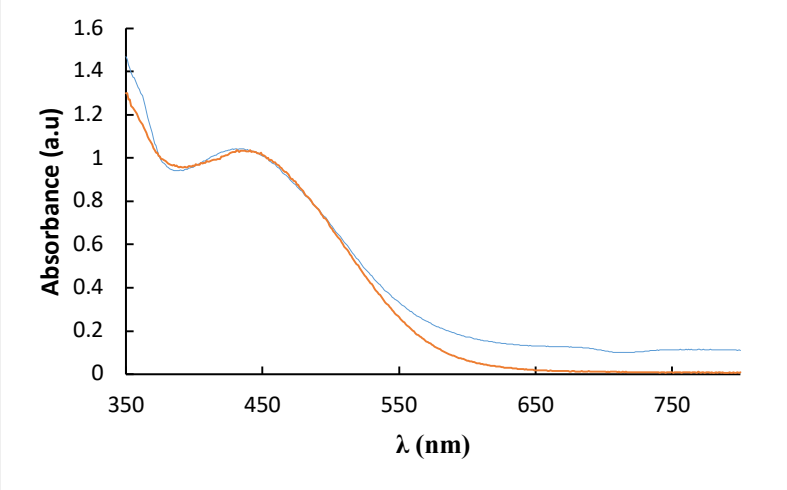

Figure S25. Visible spectra of **1˙-Br** under N_2 (orange) and under CO_2 (orange) in 0.1 M $KHCO_3$.

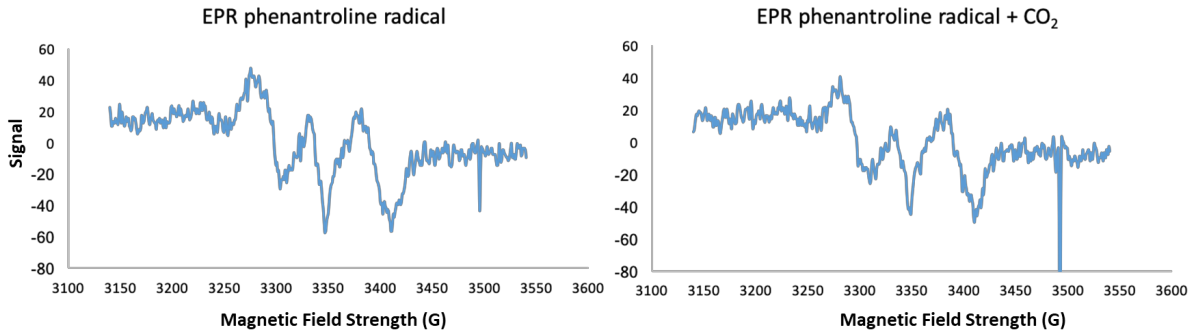

Figure S26. EPR spectra of **1˙-Br**, in a mixture of water/ethylene glycol (80/20), at 77 K, under N_2 (left) and under CO_2 (right).

The EPR spectrum of **1˙-Br** in water shows low intensity signals for both the sample under N_2 and CO_2, at 77 K. At room temperature no EPR signal was observed. The EPR signals under N_2 and CO_2 were similar indicating that the CO_2 is not reacting with **1˙-Br**.

References

[1] L. A. Summers, *Tetrahedron* **1968**, *24*, 5433–5437.
[2] L. A. Summers, *Nature* **1967**, *215*, 1410–1411.
[3] A. L. Black, L. A. Summers, *Tetrahedron* **1968**, *24*, 6453–6457.
[4] B. J. Coe, N. R. M. Curati, E. C. Fitzgerald, *Synthesis* **2006**, *2006*, 146–150.
[5] K. Jackson, J. H. Ridd, M. L. Tobe, *J. Chem. Soc. Perkin Trans. 2* **1979**, *0*, 607–610.
[6] K. P. Kuhl, E. R. Cave, D. N. Abram, T. F. Jaramillo, *Energy Environ. Sci.* **2012**, *5*, 7050–7059.
[7] P. Lobaccaro, M. R. Singh, E. L. Clark, Y. Kwon, A. T. Bell, J. W. Ager, *Phys. Chem. Chem. Phys.* **2016**, *18*, 26777–26785.
[8] S. Men, D. S. Mitchell, K. R. J. Lovelock, P. Licence, *ChemPhysChem* **2015**, *16*, 2211–2218.
[9] Y. Zhao, X. Liu, Y. Han, *RSC Adv.* **2015**, *5*, 30310–30330.
[10] A. B. Bocarsly, Q. D. Gibson, A. J. Morris, R. P. L'Esperance, Z. M. Detweiler, P. S. Lakkaraju, E. L. Zeitler, T. W. Shaw, *ACS Catal.* **2012**, *2*, 1684–1692.
[11] E. E. Barton Cole, M. F. Baruch, R. P. L'Esperance, M. T. Kelly, P. S. Lakkaraju, E. L. Zeitler, A. B. Bocarsly, *Top. Catal.* **2015**, *58*, 15–22.
[12] S. I. Rybchenko, D. Touhami, J. D. Wadhawan, S. K. Haywood, *ChemSusChem* **2016**, *9*, 1660–1669.
[13] P. K. Giesbrecht, D. E. Herbert, *ACS Energy Lett.* **2017**, *2*, 549–555.